ACS Sustainable Chemistry & Engineering

Research Article

Cite This: ACS Sustainable Chem. Eng. 2019, 7, 5921−5930

pubs.acs.org/journal/ascecg

Rational Combination of an Alabandite MnS Laminated Pyrrhotite $Fe_{1-x}S$ Nanocomposite as a Superior Anode Material for High Performance Sodium-Ion Battery

Ganesh Kumar Veerasubramani,[†] Myung-Soo Park,[†] Jin-Yi Choi,[†] Yun-Sung Lee,[‡] Sang Jae Kim,[§] and Dong-Won Kim*[,†]

[†]Department of Chemical Engineering, Hanyang University, 222 Wangsimni-ro, Seongdong-gu, Seoul 04763, Korea

[‡]Faculty of Applied Chemical Engineering, Chonnam National University, 77 Yongbong-ro, Buk-gu, Gwangju 61186, Korea

[§]Department of Mechatronics Engineering, Jeju National University, 102 Jejudaehak-ro, Jeju-si, Jeju 63243, Korea

Supporting Information

ABSTRACT: Conversion-based transition metal sulfide compounds have been considered as a promising anode material for sodium-ion batteries (SIBs). The major obstacle of these conversion-type anode materials is a large volume change in the course of sodium-ion conversion, which deteriorates their structural stability. Herein, we report a rational combination of pyrrhotite $Fe_{1-x}S$ with alabandite MnS as an anode material with the subsided structural degradation and improved storage ability for SIB. Impressively, the $Fe_{1-x}S$/MnS composite electrode initially delivered a discharge capacity of 602 mAh g^{-1} at 100 mA g^{-1} with good cycling stability and excellent rate capability, which reveals its enhanced sodium-ion storage capacity as compared to its pristine electrodes ($Fe_{1-x}S$, MnS). Electrochemical impedance spectroscopy and cyclic voltammetry analyses demonstrate the enhanced rate performance and improved cycling stability of the $Fe_{1-x}S$/MnS composite electrode as well as better pseudocapacitive contribution. The cooperative effect of the $Fe_{1-x}S$/MnS composite anode makes it as a promising anode material for SIBs.

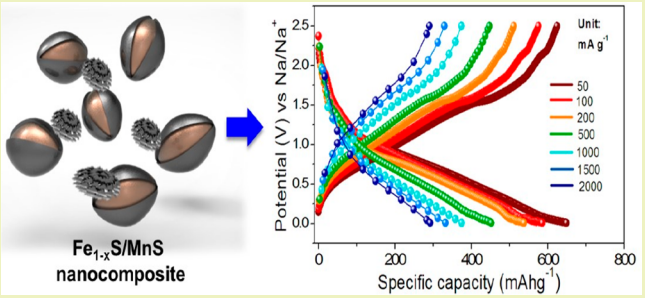

KEYWORDS: *Pyrrhotite $Fe_{1-x}S$, Alabandite MnS, Composite anode, Sodium-ion battery, Energy storage*

INTRODUCTION

Increasing environmental problems and the exhaustion of fossil fuels need the next-generation electrochemical energy conversion and storage devices.[1,2] Among various energy storage and conversion devices, lithium-ion batteries (LIBs) have engaged immense debate due to the their exceptional energy density and excellent cycle life.[3−7] Recently, with ever rising demand in the secondary batteries, sodium-ion based batteries (SIBs) have been received expanding demand by many researchers by cause of their analogous energy storage mechanism to the LIBs. In addition, the lower cost of sodium by its high abundance and widespread nature can advance their substantial grid based energy storage systems in near future.[8−10] However, the development of SIBs is still hindered by their inferior restraints, such as higher molar mass and larger ionic radius than lithium.[11−13] To meet the commercial requirements, it is essential to flourish the high-capacity electrode materials by surviving with its initial capacity for long lasting and satisfying rate capability.[14,15] Metal sulfides such as MoS_2, Co_9S_8, FeS_2, Sb_2S_3, and SnS have been attracted as an encouraging anode materials in the secondary batteries, especially in SIBs.[8,9,11,16−20] Among them, iron sulfide is being studied as a suitable candidate by reason for its high theoretical capacity, environmental benevolence, and inexpensiveness.[21−23] Furthermore, FeS_2 has been used as an electrode material in the commercialized primary cell.[24,25] However, the main concern of FeS_2 is the large volume change occurred during continuous sodium insertion and extraction, resulting in poor electrochemical performance for rechargeable battery. Recently, the nonstoichiometric iron sulfides ($Fe_{1-x}S$) have drawn a lot of attention and studied as the potential electrode material for SIB anodes. Li et al. reported a scalable preparation of $Fe_{1-x}S$ with high discharge capacity and unprecedented rate capability by pseudocapacitance contribution.[26] Xiao et al. investigated a sodium-ion storage characteristic of the CNT enclosed $Fe_{1-x}S$ composite with a reversible capacity of 448 mAh g^{-1} after 200 cycles.[27] Pan et al. reported a $Fe_3O_4/Fe_{1-x}S@C@MoS_2$ composite material delivering a specific capacity of 650 mAh g^{-1} at 100 mA g^{-1}.[28] As like other iron sulfides, the long-term stability and rate efficiency of $Fe_{1-x}S$ are not good due to its structural degradation by large

Received: November 13, 2018
Revised: January 23, 2019
Published: January 29, 2019

DOI: 10.1021/acssuschemeng.8b05904
ACS Sustainable Chem. Eng. 2019, 7, 5921−5930

Scheme 1. Schematic Description of the Preparation of $Fe_{1-x}S$/MnS Nanocomposites

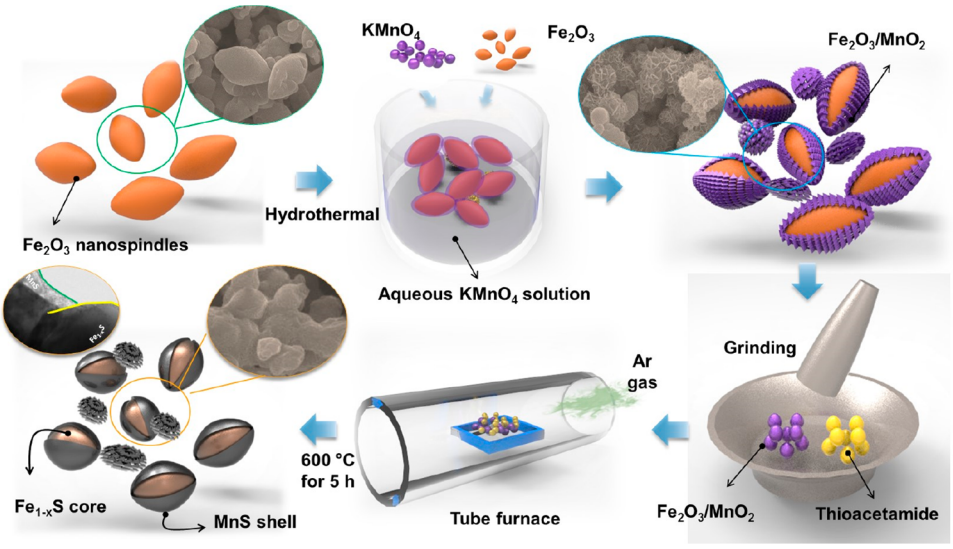

volume expansion. On the other hand, MnS is a relatively low-cost metal chalcogenide and has been studied as an effective electrode material (with a high theoretical capacity of 616 mAh g^{-1}) for LIBs.[29,30] Recently, Gao et al. presented that the hybrid composed of MnS and carbon fiber exhibited a low specific capacity with relatively better long-term stability and rate efficiency.[31] Gao et al. reported the ameliorated electrochemical performance of rod-like carbon-coated MnS synthesized from metal organic frameworks as an anode material for SIBs with enhanced cycling and rate capability.[32] However, its low electronic conductivity, low charge transfer rate, and large volume change lead to poor electrochemical performance.[32,33] To mitigate the large volume change of the metal sulfides, many approaches including carbon coating, graphene encapsulation, and hybrid with other metal sulfides have been investigated.[8,11,18−20,22,23] According to the previous studies, the composite of two different metal sulfides could enhance the electrochemical output in terms of better durability, high discharge capacity, and rate capability. Geng et al. reported the improved cycling performance of Co_9S_8/MoS_2 yolk−shell electrodes for SIBs even though the pristine Co_9S_8 and MoS_2 exhibited poor cycling stability.[17] Recently, rate capability of SIBs was enhanced by utilizing Co_9S_8/MoS_2 yolk−shell with the N-doped carbon composite.[34] Tan et al. reported the CoS/NiS composite anchored on reduced graphene oxide for LIBs.[35] More importantly, Zhao et al. reported the combination of MnS with Fe to form $Fe_xMn_{1-x}S$ solid solution to improve the cycling stability in comparison with their pristine MnS and FeS.[36] However, the hybrid structures of $Fe_{1-x}S$ with other phases of metal sulfides are very limited. It motivated us to study on the combination of pyrrhotite $Fe_{1-x}S$ with alabandite MnS, which may provide cooperative benefits that manifest the whole structural advantages over the individual components. Our results in this study demonstrate that the $Fe_{1-x}S$/MnS composite electrode exhibits improved rate and cycling performance compared to their individual materials.

EXPERIMENTAL SECTION

Preparation of Fe_2O_3 Nanospindles. Fe_2O_3 nanospindles were synthesized via one pot and facile hydrothermal method.[37] Briefly, a proper amount of $FeCl_3$ was dissolved in deionized water. Few amounts of urea and ethylene diol were added into the solution as a protective agent, and the mixture was kept at vigorous stirring for several minutes. Then, the prepared solution was shifted to an 80 mL autoclave (Teflon-lined) and heated to 180 °C for 12 h in the hot oven. Subsequently, the autoclave was placed for cooling to normal temperature after reaction. Afterward, the collected product was washed and finally dried at 80 °C.

Preparation of Fe_2O_3/MnO_2 Nanocomposites. A proper amount of the Fe_2O_3 nanospindles was dispersed in solution containing 50 mmol of $KMnO_4$. The mixed solution was placed for stirring and sonication. Immediately, the solution was subjected to a hydrothermal reaction at 160 °C for 12 h. The obtained precipitate was collected and washed with distilled water and ethanol. For comparison, MnO_2 was prepared without the addition of Fe_2O_3.

Preparation of $Fe_{1-x}S$/MnS Nanocomposites. The prepared Fe_2O_3/MnO_2 nanocomposites were mixed with thioacetamide as sulfur source in the weight ratio of 1:3 and grinded well using agate mortar. The mixed powder was transferred to the alumina boat and kept inside the tube furnace. The sulfurization reaction was carried out by heating the furnace to 600 °C for 5 h at Ar atmosphere (with 1 °C min^{-1} ramping rate)to obtain $Fe_{1-x}S$/MnS (1:1) nanocomposite. For simplicity, this composite will be denoted as $Fe_{1-x}S$/MnS. For comparison, the pristine $Fe_{1-x}S$ and MnS were prepared using the same procedure by mixing thioacetamide with the prepared Fe_2O_3 and MnO_2, respectively. Other $Fe_{1-x}S$/MnS (2:1) and $Fe_{1-x}S$/MnS (1:2) composites were also prepared by varying the initial precursors.

Material Characterization. X-ray diffractometer (D8 Bruker) was used to collect X-ray diffraction pattern of all the samples with wavelength of 1.5405 Å (Cu Kα radiation). Raman spectroscopy was used to investigate the bonding nature of the prepared materials by Dongwoo optron (Model: MonoRa 780i). Morphology of all samples was examined by scanning electron microscope (SEM, NOVA Nano SEM-450) furnished with energy dispersive X-ray spectroscopy (EDS) and high-resolution transmission electron microscope (HR-TEM, JEOL, JEM 2100F) equipped with mapping technique. Oxidation state of the prepared material was studied using X-ray photoelectron spectroscopy (XPS) using a VG Multilab ESCA System (220i) with Mg/Al Kα radiation.

Electrochemical Measurements. A slurry was prepared for making electrode by grinding the synthesized $Fe_{1-x}S$, MnS, and $Fe_{1-x}S$/MnS as an active material, carboxy methyl cellulose (CMC) as binder and Super-P as a conductive agent at 70:15:15 (weight ratio) using water as the solvent. Subsequently, the slurry was coated onto the Cu foil using doctor blade to make electrode and dried in an oven at 80 °C for 12 h at vacuum condition. The mass of active material was measured to be about 3.0 mg cm^{-2}. To investigate the electrochemical performance of the prepared electrodes, a coin cell (CR2032) was made using a sodium foil (Alfa Aesar 99%) at one side and the prepared

DOI: 10.1021/acssuschemeng.8b05904
ACS Sustainable Chem. Eng. 2019, 7, 5921−5930

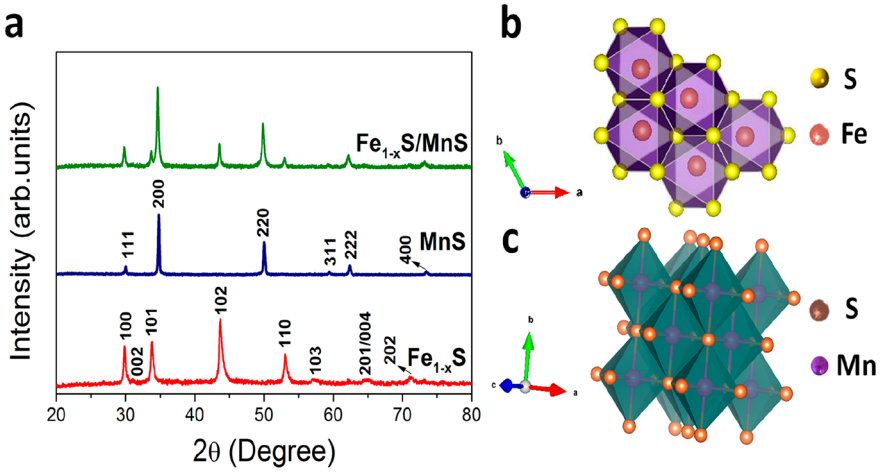

Figure 1. (a) XRD patterns of $Fe_{1-x}S$, MnS, and $Fe_{1-x}S$/MnS nanocomposite. Crystal structures of (b) $Fe_{1-x}S$ and (c) MnS.

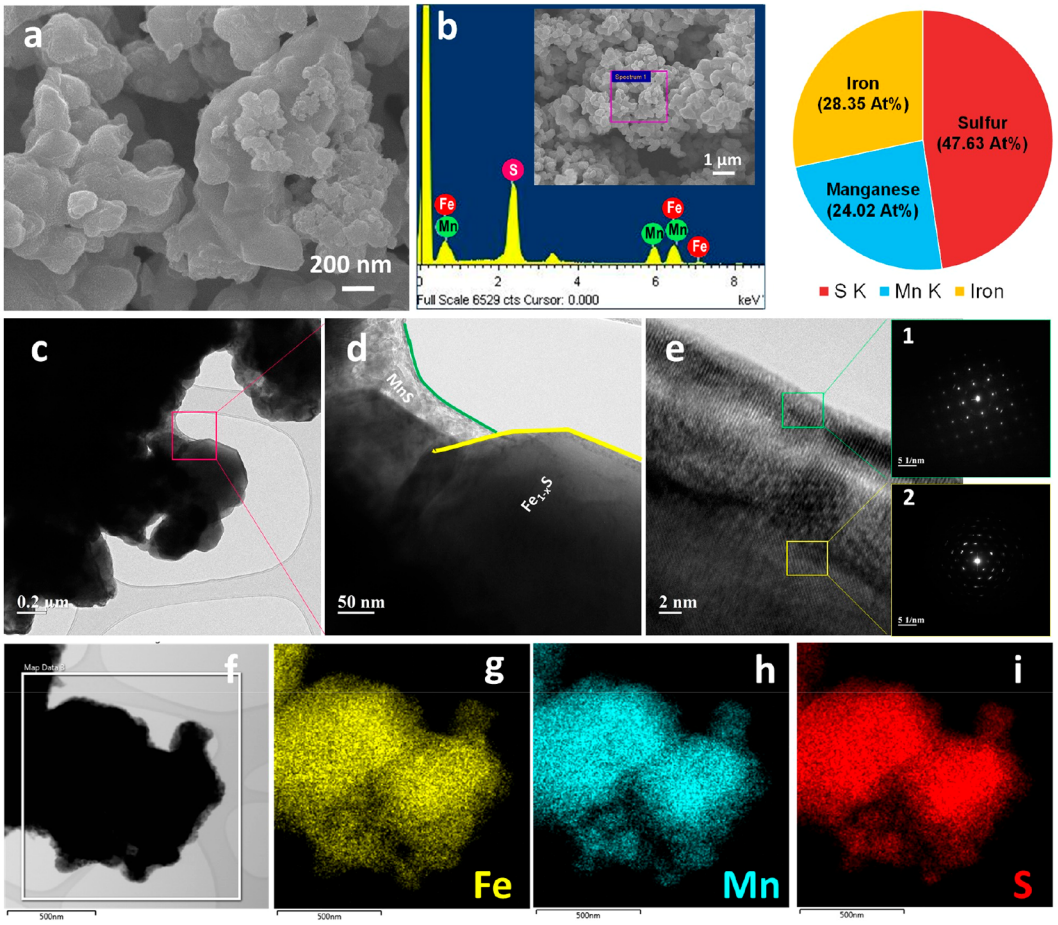

Figure 2. (a) FE-SEM image, (b) EDS result, (c, d) TEM images with different magnifications of the $Fe_{1-x}S$/MnS nanocomposite. (e) HR-TEM image with SAED patterns showing (1) $Fe_{1-x}S$ and (2) MnS in the nanocomposite. (f) TEM image and elemental mapping images of (g) Fe, (h) Mn, and (i) S atoms in the $Fe_{1-x}S$/MnS nanocomposite.

electrode at another side as a working electrode with a glass fiber as a separator (Whatman). Liquid electrolyte solution was then injected into the coin-cell. The electrolyte solution was prepared by dissolving 1.0 M $NaClO_4$ in the mixed solvent of ethylene carbonate and propylene carbonate (volume ratio: 1:1) containing 10 wt % fluoroethylene carbonate. The content of water in the electrolyte was measured to be <20 ppm by Karl Fisher titration using Mettler-Toledo Coulometer. All the coin-cells were fabricated inside glovebox at argon gas atmosphere. CH instrument (CHI 600D) was used to perform electrochemical impedance spectroscopy and cyclic voltammetry at 25 °C. Battery cycler (WBCS 3000, WonA Tech Co., Ltd.) was used to conduct the charge and discharge cycling test of the cells at 25 °C.

RESULTS AND DISCUSSION

Hydrothermal reaction and sulfidation were used to synthesize the $Fe_{1-x}S$/MnS nanocomposite, as presented in Scheme 1. The prepared Fe_2O_3 nanospindles was hydrothermally treated with

DOI: 10.1021/acssuschemeng.8b05904
ACS Sustainable Chem. Eng. 2019, 7, 5921−5930

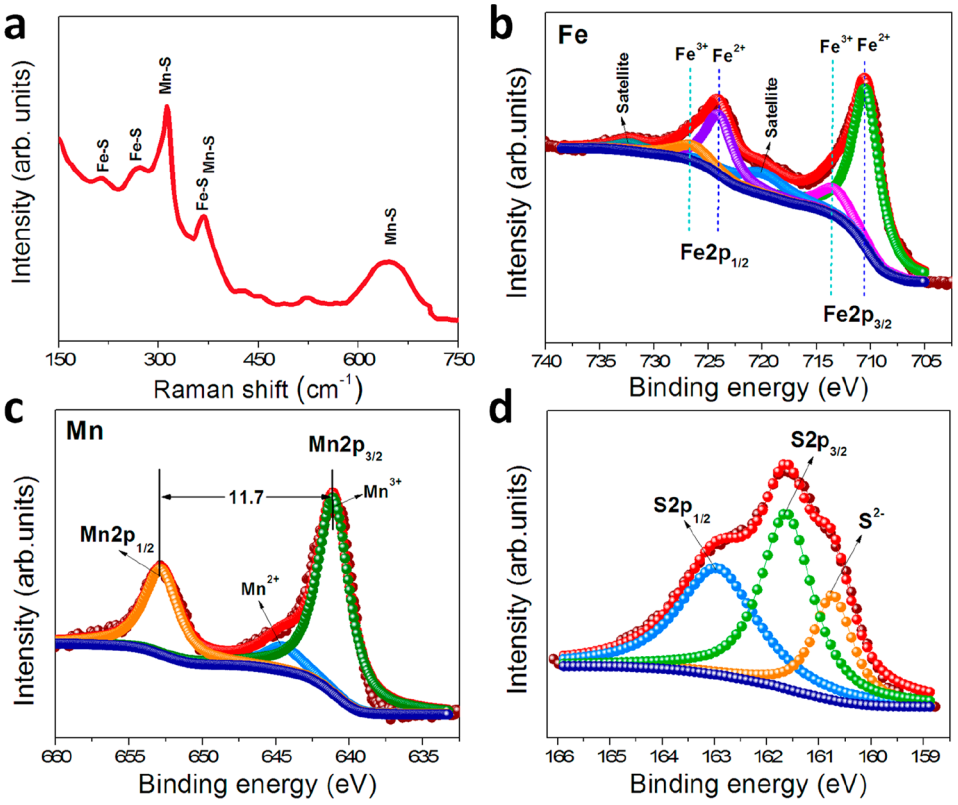

Figure 3. (a) Raman spectrum of the $Fe_{1-x}S$/MnS nanocomposite. XPS spectra of (b) Fe 2p, (c) Mn 2p, and (d) S 2p core-level spectrum of the $Fe_{1-x}S$/MnS nanocomposite.

$KMnO_4$ solution to form Fe_2O_3/MnO_2 composite. This composite was subjected to the sulfurization reaction by grinding with thioacetamide to finally form the $Fe_{1-x}S$/MnS nanocomposite.

Figure S1a–c show the XRD patterns of Fe_2O_3, MnO_2, and Fe_2O_3/MnO_2 composite materials. All the crystalline peaks in the Fe_2O_3 material correspond to the planes for hematite phase of α-Fe_2O_3 (JCPDS: 33–0664) without any other impurities. The additional peaks were observed at the angle of 12.5°, 24.9°, 36.7°, and 65.7°, when introducing MnO_2 into Fe_2O_3. They can be indexed to the (001), (002), (100), and (020) planes of Birnessite δ-MnO_2. The Fe_2O_3/MnO_2 composite was pulverized with thioacetamide and subjected to sulfidation reaction at high temperature. During the sulfidation reaction, Fe_2O_3 was reduced to Fe_3O_4, wherein Fe_3O_4 contains two oxidation states of Fe^{2+} and Fe^{3+}. These two ions can be coordinated with sulfur atom from thioacetamide to form a complex structure followed by the cleavage in thioacetamide to produce the non-stoichiometric $Fe_{1-x}S$.[38] Similarly, MnO_2 was initially reduced to Mn_3O_4 and further reduced to MnO during high temperature reaction. Mn^{2+} ions in MnO can coordinate with sulfur atoms in thioacetamide and followed by the formation of MnS by the cleavage of coordinated bonds in thioacetamide under inert atmosphere.[38]

Figure 1a shows the XRD patterns of the $Fe_{1-x}S$, MnS, and $Fe_{1-x}S$/MnS composite. All the diffraction peaks observed in $Fe_{1-x}S$ material can be assigned to the hexagonal phase of pyrrhotite $Fe_{1-x}S$ without any other impurities or phases.[25] The crystalline peaks at 29.9°, 31.0°, 33.7°, 43.7°, 53.0°, 57.1°, 65.1°, and 71.3° can be indexed to the (100), (002), (101), (102), (110), (103), (201/004), and (202) planes, respectively, which correspond to the JCPDS card no. 29–0726. In the case of the $Fe_{1-x}S$/MnS composite, there are some sharp peaks that can be identified as the cubic phase of MnS (space group of $Fm\bar{3}m$). These peaks could be found in the pristine MnS and the obtained peaks were indeed matched with the standard JCPDS file no. 01–1089.[33] Figure S1d shows the XRD patterns of the $Fe_{1-x}S$/MnS (2:1 and 1:2) composites. As seen in the figure, the $Fe_{1-x}S$/MnS (2:1) composite exhibited similar peaks with $Fe_{1-x}S$/MnS (1:1) composite; however, some impurity peaks corresponding to the elemental Fe and unreacted Fe_3O_4 were observed. On the other hand, the $Fe_{1-x}S$/MnS (1:2) composite showed more dominant MnS peak with unreacted Mn_3O_4.[39] Figure 1b,c shows the crystal structures of the corresponding $Fe_{1-x}S$ and MnS, respectively. According to their crystal structures, the S ion resided in the trigonal prismatic sites, whereas Fe ions occupied in the octahedral sites in the pyrrhotite $Fe_{1-x}S$. Mn ions occupy the octahedral sites that are surrounded by six sulfur atoms in the alabandite MnS.

Figure S2 shows the FE-SEM images of the hydrothermally prepared Fe_2O_3, MnO_2, and Fe_2O_3/MnO_2 composites. As can be seen in the images, the nanospindle and nanoflower-like morphologies are observed for Fe_2O_3 and MnO_2, respectively. In the case of Fe_2O_3/MnO_2 composite, two materials are uniformly interconnected with each other. After sulfidation at 600 °C under inert atmosphere with thioacetamide as sulfur source, both spindle and flower-like morphologies were destroyed, and the nanoparticle-like structure was formed by complexation of Fe and Mn with sulfur coordination for the prepared $Fe_{1-x}S$/MnS composite, as shown in Figure 2a. To investigate the composition of each element in the $Fe_{1-x}S$/MnS composite, EDS was performed with FE-SEM image, as presented in Figure 2b. It is found that the Fe, Mn, and S atoms are consistently scattered in the composite with expected atomic ratio. Figure

DOI: 10.1021/acssuschemeng.8b05904
ACS Sustainable Chem. Eng. 2019, 7, 5921–5930

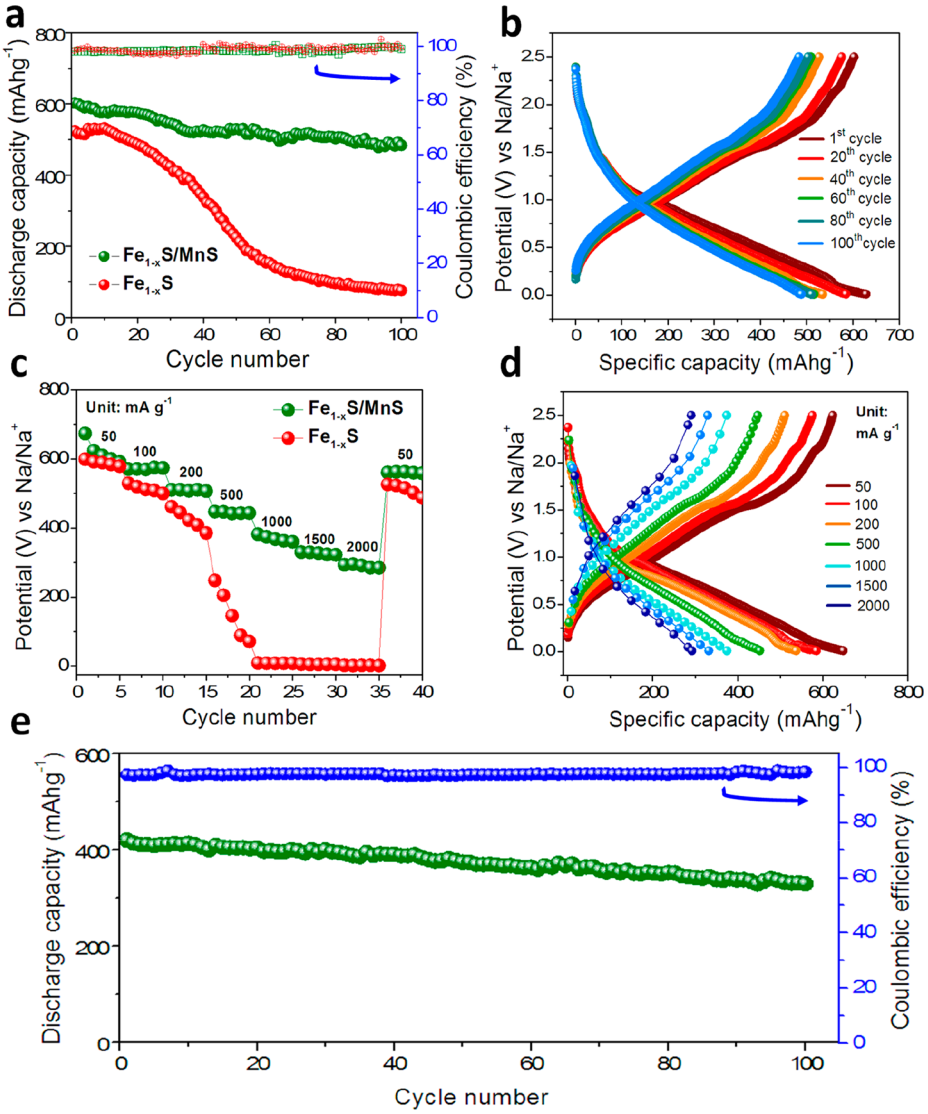

Figure 4. (a) Cycling performance of the $Fe_{1-x}S$ and $Fe_{1-x}S$/MnS composite anodes, (b) charge/discharge graph of the $Fe_{1-x}S$/MnS composite anode at 100 mA g^{-1}, (c) rate performance of the $Fe_{1-x}S$ and $Fe_{1-x}S$/MnS composite anodes, (d) charge/discharge graph of the $Fe_{1-x}S$/MnS composite electrode at different current densities, and (e) cycling stability of the $Fe_{1-x}S$/MnS composite electrode at 1000 mA g^{-1}. Cycle test was carried out after two preconditioning cycles at 50 mA g^{-1}.

2c,d shows the TEM images of the $Fe_{1-x}S$/MnS composite at different magnifications. As shown in Figure 2d, the pyrrhotite $Fe_{1-x}S$ nanoparticle was covered with sheet-like alabandite MnS material. The HR-TEM image with SAED patterns in Figure 2e clearly confirms the presence of $Fe_{1-x}S$ and MnS in the composite with highly crystalline nature. Moreover, the presence of all the atoms such as Fe, Mn, and S on the surface of the particles was proved by the elemental mapping images presented in Figure 2f–i.

Raman spectroscopy can be used to investigate the bonding nature of the materials. Figure 3a shows the Raman spectrum of the Fe_{1-x} S/MnS composite. The peaks observed at 213 and 272 cm^{-1} can be associated with the symmetric and asymmetric stretching vibrations of Fe–S in the Fe_{1-x} S material, respectively.[40,41] On other hand, the bands at 314 and 370 cm^{-1} are analogous to the transverse optical phonon (TO) vibration and longitudinal optical phonon (LO) vibration, respectively, along with the strong photoluminescence band at 645 cm^{-1} in MnS material.[42−44]

Figure 3b–d show the XPS spectra of the $Fe_{1-x}S$/MnS composite. As shown in Fe 2p core-level spectrum, the peak could be separated by Fe $2p_{1/2}$ and Fe $2p_{3/2}$ in higher and lower binding energy levels respectively. These two core-levels could be deconvoluted to provide two oxidation states of Fe^{2+} (724.2 eV) and Fe^{3+} (726.7 eV) in Fe $2p_{1/2}$, whereas Fe^{2+} (710.5 eV) and Fe^{3+} (713.5 eV) in Fe $2p_{3/2}$, respectively.[25,45] In addition, satellite peaks were observed at the higher binding energies of two Fe 2p core-level. Mn 2p core-level spectrum was also divided into Mn $2p_{1/2}$ and Mn $2p_{3/2}$ at the higher and lower binding energy levels respectively. The spin–orbit splitting of 11.7 eV for both Mn 2p core-level further confirms the presence of MnS.[46] One more peak observed around 645 cm^{-1} can be ascribed to the complex of Mn^{3+} ion with other atoms.[44,45] As observed in Figure 3d, the S 2p spectrum could be deconvoluted into the three peaks, 162.9 eV for S $2p_{1/2}$, 161.6 eV S $2p_{3/2}$, and 160.8 eV for metal sulfides.

The electrochemical characteristics of the $Fe_{1-x}S$, MnS, and $Fe_{1-x}S$/MnS composite was evaluated. Figure 4a shows the discharge capacities of the $Fe_{1-x}S$ and $Fe_{1-x}S$/MnS composite

DOI: 10.1021/acssuschemeng.8b05904
ACS Sustainable Chem. Eng. 2019, 7, 5921−5930

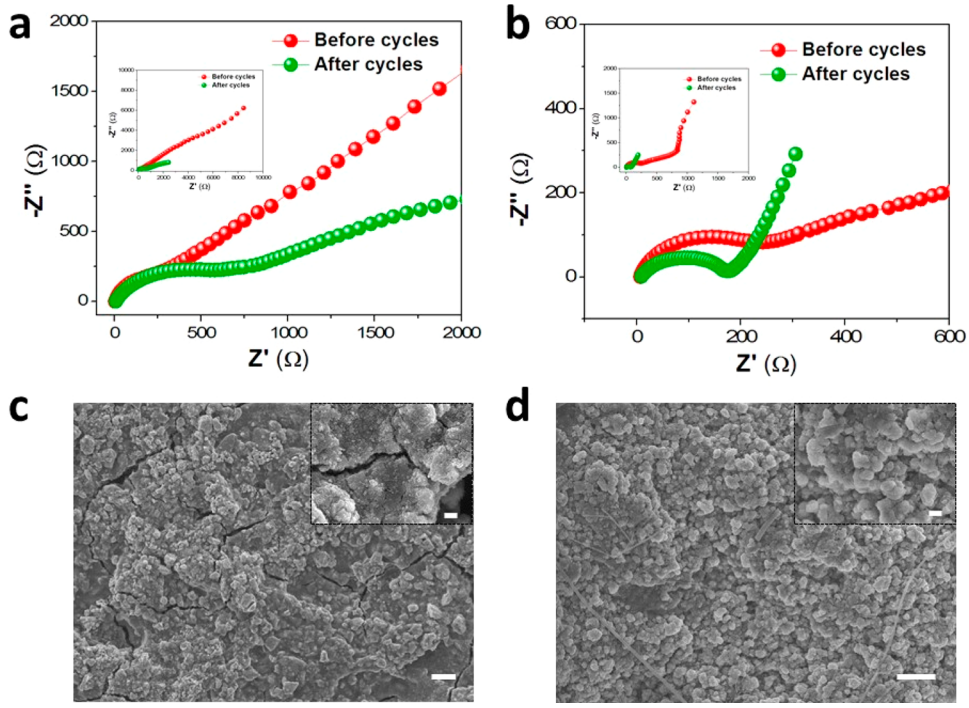

Figure 5. AC impedance spectra of (a) $Fe_{1-x}S$ and (b) $Fe_{1-x}S$/MnS composite electrodes before and after cycles at 25 °C. SEM images of (c) $Fe_{1-x}S$ and (d) $Fe_{1-x}S$/MnS composite electrodes at 100 mA g^{-1} after 100 cycles. The scale bars correspond to 10 and 1 μm for image and inset, respectively.

with cycling, which were obtained at the current density of 100 mA g^{-1} after two preconditioning cycles at 50 mA g^{-1}. A maximum discharge capacity of 602 mAh g^{-1} was obtained for the $Fe_{1-x}S$/MnS composite electrode. On the other hand, the $Fe_{1-x}S$ electrode delivered a discharge capacity of 524.5 mAh g^{-1} initially and the MnS electrode delivered only 152 mAh g^{-1} (Figure S3a). Figure 4b shows the typical charge and discharge curves of the $Fe_{1-x}S$/MnS composite electrode in the potential range of 0.01−2.5 V at 100 mA g^{-1}. The Coulombic efficiency of the $Fe_{1-x}S$/MnS composite electrode after two preconditioning cycles was 95.7%, which is relatively higher than pristine $Fe_{1-x}S$ (94.2%) and MnS (89.1%) electrodes. Its discharge capacity was preserved to 484 mAh g^{-1} even after 100 continuous charge/discharge cycles. In case of pristine $Fe_{1-x}S$ and MnS electrodes, the drastic capacity loss was observed after 100 cycles, and their discharge capacities were dropped to 76 and 32 mAh g^{-1} for the $Fe_{1-x}S$ and MnS electrodes, respectively. Such a large capacity decline is related to the extensive volume expansion, cracks in the electrode, and slow kinetics of the electrode material during conversion reaction.[32,33] Figure 4c,d and Figure S3b present the rate capability of different electrodes at various current densities. Clearly, the $Fe_{1-x}S$/MnS composite showed much better high rate performance than the $Fe_{1-x}S$ and MnS electrodes. The $Fe_{1-x}S$/MnS composite electrode delivered a relatively high discharge capacity of 290 mAh g^{-1} at 2000 mA g^{-1}. A discharge capacity of 561 mAh g^{-1} at 50 mA g^{-1} was recovered after high-current cycling, which demonstrates good rate performance and cycling stability of the $Fe_{1-x}S$/MnS composite electrode. Further, the long-term durability of the $Fe_{1-x}S$/MnS composite electrode was evaluated at high current density of 1000 mA g^{-1}. As shown in Figure 4e, the $Fe_{1-x}S$/MnS composite electrode delivered a discharge capacity of 329 mAh g^{-1} after 100 continuous cycles and exhibited good capacity retention during cycling. It is believed that the interconnection of MnS with $Fe_{1-x}S$ allows good cycling stability and enhanced high-rate performance. In addition, the presence of MnS in the $Fe_{1-x}S$/MnS composite electrode may reduce the volume expansion of $Fe_{1-x}S$ during conversion reaction, resulting in the improvement of cycling stability and rate capability. For comparison, the electrochemical performance of the $Fe_{1-x}S$/MnS (2:1) and $Fe_{1-x}S$/MnS (1:2) composites was evaluated, and the results are presented in Figure S4. The initial discharge capacities of $Fe_{1-x}S$/MnS (2:1) and $Fe_{1-x}S$/MnS (1:2) were almost the same irrespective of composite ratio; however, the values were lower than that of $Fe_{1-x}S$/MnS (1:1) composite. The lower initial discharge capacities might be due to the presence of the impurities in the active materials. With respect to cycling stability and rate performance, the $Fe_{1-x}S$/MnS (2:1) composite exhibited better performance than $Fe_{1-x}S$/MnS (1:2) composite, which can be ascribed to the presence of higher amount of $Fe_{1-x}S$ in the $Fe_{1-x}S$/MnS (2:1) composite. These results suggest that other combinations of $Fe_{1-x}S$ and MnS show poor cycling performance than $Fe_{1-x}S$/MnS (1:1) composite due to the presence of oxide-based and elemental impurities, which causes some side reactions leading to the lower capacity and capacity fading.

To examine the origin for differences in the cycling performance of various electrodes, the AC impedance spectra of the electrodes were obtained before and after repeated cycles, and the results are presented in Figure 5 and Figure S3c. In case of the $Fe_{1-x}S$ electrode, the charge transfer resistance was drastically increased after 100 cycles, which arose from the loss of electrode conductivity by relentless volume change of $Fe_{1-x}S$ particles during continuous cycling. Similar behavior was observed in the MnS electrode, as depicted in Figure S3c. In contrast, the charge transfer resistance was decreased after 100 cycles in the $Fe_{1-x}S$/MnS composite electrode. This is due to the fact that the conductivity is enhanced and the structural degradation of the $Fe_{1-x}S$ can be suppressed during conversion reaction by the presence of MnS with $Fe_{1-x}S$.

DOI: 10.1021/acssuschemeng.8b05904
ACS Sustainable Chem. Eng. 2019, 7, 5921−5930

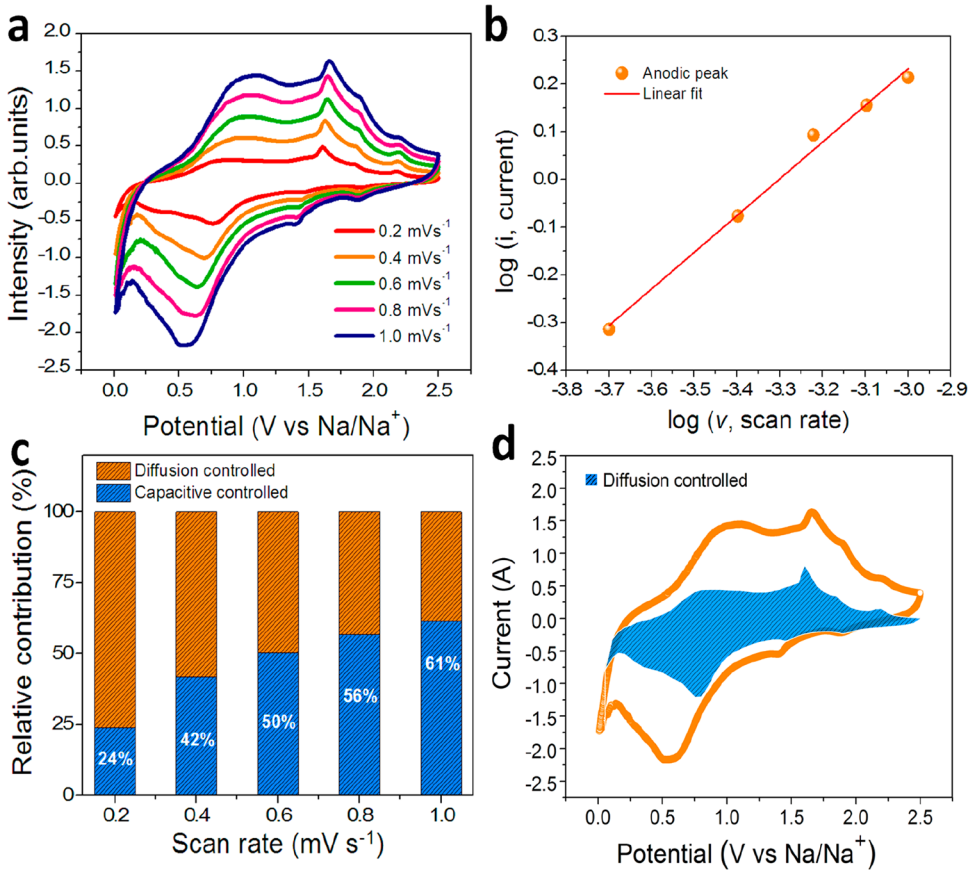

Figure 6. (a) Cyclic voltammograms at various scan rates scanning between 0.2 and 1.0 mV s^{-1}, (b) the plot of log *i* vs log *v* linear fit, (c) relative contribution from the diffusion-controlled (orange) and capacitive-controlled (blue) processes at various scan rates, and (d) cyclic voltammograms with the diffusion-controlled (blue area) and capacitive-controlled process (empty area) at a scan rate of 1 mV s^{-1} for the $Fe_{1-x}S$/MnS composite electrode.

The *ex-situ* morphological analyses of the $Fe_{1-x}S$, MnS, and $Fe_{1-x}S$/MnS electrodes after cycling were investigated using FE-SEM, and the results are presented in Figure 5c,d and Figure S3d. As shown in the figures, the pristine $Fe_{1-x}S$ and MnS electrodes showed many cracks on their surface after 100 cycles. This is because the pristine $Fe_{1-x}S$ and MnS electrodes could not sustain over the large volume strain in the course of continuous de/sodiation processes. The cracks in the electrode cause the loss of electric contact between current collector, active materials and conducting carbons, which led to the increase of interfacial resistances during cycling, as discussed in the AC impedance results. On the other hand, the $Fe_{1-x}S$/MnS composite electrode showed little cracks or damage, indicating that the composite electrode can able to constrain the volume changes in the electrode during de/sodiation.

Cyclic voltammetry was carried out to investigate the electrochemical characteristics of the $Fe_{1-x}S$/MnS composite electrode. Figure S5 shows the CV curves of the $Fe_{1-x}S$/MnS composite electrode at 0.1 mV s^{-1} in the potential range between 0.01 and 2.5 V during initial three cycles. During initial cathodic scan, the peaks observed at 0.13 and 0.45 V are related to the multistep electrochemical reduction. It might be accompanied by the generation of sodium rich phases by the conversion reaction between the sodium metal with $Fe_{1-x}S$ and MnS.[23,47−49] The cathodic current is also arising from the generation of solid electrolyte interphase (SEI) layer by reductive decomposition of the electrolyte. The anodic peaks during the anodic scan are related to the desodiation process. The sodium storage mechanism can be explained as following electrochemical reactions.[25]

$$Fe_{1-x}S + Na^+ + 2e^- \rightarrow Na_2S + Fe \quad (1)$$

$$Na_2S + Fe \leftrightarrow Na_aFe_{1-x}S_b + 2Na^+ + 2e^- \quad (2)$$

$$MnS + Na^+ + 2e^- \leftrightarrow Na_2S + Mn \quad (3)$$

After initial activation process, the area under the CV curves is almost same, which implies the good reversibility and cycling stability of the $Fe_{1-x}S$/MnS composite electrode. Cyclic voltammetry of the $Fe_{1-x}S$/MnS electrode was performed from 0.01 to 2.5 V at scan rates of 0.2 to 1.0 mV s^{-1}, and the resulting CV curves are presented in Figure 6a. When increasing the scan rate, all anodic and cathodic peaks were almost identical and slightly shifted toward higher and lower potentials, respectively, because of the electrode polarization.[50] According to the previous literature, the total charge capacity can be differentiated into three parts:[51−53] (i) the contribution of faradaic current from the diffusion-controlled process by the Na-ion conversion reaction, (ii) the contribution from the charge transfer reaction occurred at the surface of the electrode in the atomic level, called as pseudocapacitance, and (iii) the nonfaradaic process from the electric double layer capacitance. The capacitive and pseudocapacitive contribution cannot be distinguished; however, the total contribution could be evaluated by the relationship between the peak current (*i*) vs scan rate (*v*) from the CV curves. The respective contribution of

DOI: 10.1021/acssuschemeng.8b05904
ACS Sustainable Chem. Eng. 2019, 7, 5921−5930

the capacitive and diffusion controlled process to the total capacity was estimated according to the power law. The expression of peak current to the scan rate can be given as $i_p = a \times \nu^b$, as shown in Figure 6b, where i_p is the "peak current", ν is the "scan rate", and a and b are the "adjustable parameters".[53] From this, the determined "b" values for an anodic and cathodic peaks are 0.84 and 0.77, respectively, indicating the dominance of pseudocapacitive contribution in the total capacity. In order to explain the charge storage nature, the power law was modified to the following eq 4,

$$i_p = k_1\nu + k_2\nu^{1/2} \quad (4)$$

where $k_1\nu$ and $k_2\nu^{1/2}$ are the contribution of current from capacitive and diffusive processes. The k_1 and k_2 in the equation 4 represents the value of slope and intercept calculated from the $i_p\nu^{-1/2}$ versus $\nu^{1/2}$ linear fit plot. Thus, the eq 4 was used to estimate the relative contribution of diffusion/capacitive behavior, and the results are depicted in Figure 6c. The diffusion-controlled process was dominated in the charge storage capacity at lower scan rates. With increasing the scan rates, the diffusion-controlled contribution declines and the capacitive contribution gradually increased. Figure 6d shows the CV curves of the $Fe_{1-x}S$/MnS composite electrode at 1.0 mV s^{-1}, which demonstrate the capacitive and diffusion-controlled contribution to the total capacity. In this figure, the area highlighted in blue color inside the CV curve represents the diffusion-controlled faradaic contribution. The difference between the total capacity and the faradaic contribution provides the capacitive contribution.

Overall, the enhanced sodium storage capability of the $Fe_{1-x}S$/MnS composite electrode can be explained as follows, (i) combining $Fe_{1-x}S$ and MnS into rationally constructed composite architectures could supply synergistic benefits; (ii) a hierarchical composite designed with different metal sulfides could not only provide affluent redox chemistry, but also synergistically manifest the merits of individual component; (iii) the capacity fading could be mitigated by controlling the structural degradation of one another compared to individual component through the combination of two different metal sulfides; and (iv) the pseudocapacitive contribution could be improved.[17,54,55] Such an enhanced capacitive contribution from the unique structural characteristic and cooperative effect of $Fe_{1-x}S$/MnS composite electrode might be a main reason for the improved electrochemical performance.

CONCLUSIONS

We successfully prepared the $Fe_{1-x}S$/MnS composite material via hydrothermal and sulfidation reaction. Two different metal sulfides, $Fe_{1-x}S$ and MnS, with different crystal structures could be obtained by sulfidation of the Fe_2O_3/MnO_2 composite. Compared to the pristine $Fe_{1-x}S$ and MnS electrodes, the $Fe_{1-x}S$/MnS composite electrode presented long life span and enhanced rate capability. A maximum initial discharge capacity of 602 mAh g^{-1} was obtained at 100 mA g^{-1} and it maintained to 484 mAh g^{-1} with a capacity retention of >80% after 100 cycles. The cycling stability of the $Fe_{1-x}S$/MnS composite electrode was 4× higher than the $Fe_{1-x}S$ and MnS electrodes, arising from the structural stability by accommodating volume strain during cycling. This exaggerated performance of the rationally designed $Fe_{1-x}S$/MnS composite electrode can be explained by the capacitive contribution at high current rates. Our results demonstrate that the prepared $Fe_{1-x}S$/MnS composite material can be applied as a promising anode material for sodium-ion batteries.

ASSOCIATED CONTENT

Supporting Information

The Supporting Information is available free of charge on the ACS Publications website at DOI: 10.1021/acssuschemeng.8b05904.

XRD patterns and FE-SEM images of Fe_2O_3, MnO_2, Fe_2O_3/MnO_2, and $Fe_{1-x}S$/MnS (2:1 and 1:2) nanocomposites. Cycling performance, AC impedance spectra, and ex situ SEM image of the MnS electrode. Cycling performance of the $Fe_{1-x}S$/MnS (2:1 and 1:2) composite electrodes. Cyclic voltammograms of the $Fe_{1-x}S$/MnS composite electrode (PDF).

AUTHOR INFORMATION

Corresponding Author

*Tel.: +82 2 2220 2337. Fax: +82 2 2298 4101. E-mail: dongwonkim@hanyang.ac.kr.

ORCID

Ganesh Kumar Veerasubramani: 0000-0002-3177-934X
Yun-Sung Lee: 0000-0002-6676-2871
Sang Jae Kim: 0000-0002-5066-2622
Dong-Won Kim: 0000-0002-1735-0272

Notes

The authors declare no competing financial interest.

ACKNOWLEDGMENTS

This work was supported by the National Research Foundation of Korea (NRF) funded by the Korea Government (2017R1C1B2012700) and the Basic Science Research Program of NRF, funded by the Ministry of Science, ICT, and Future Planning (2016R1A4A1012224).

REFERENCES

(1) Simon, P.; Gogotsi, Y. Materials for Electrochemical Capacitors. *Nat. Mater.* **2008**, *7*, 845−854.
(2) Schlapbach, L.; Zuttel, A. Hydrogen-storage Materials for Mobile Applications. *Nature* **2001**, *414*, 353−358.
(3) Armand, M.; Tarascon, J. Building Better Batteries. *Nature* **2008**, *451*, 652−657.
(4) An, Y.; Fei, H.; Zeng, G.; Ci, L.; Xiong, S.; Feng, J.; Qian, Y. Green, Scalable and Controllable Fabrication of Nanoporous Silicon from Commercial Alloy Precursors for High-Energy Lithium-Ion Batteries. *ACS Nano* **2018**, *12*, 4993−5002.
(5) Bruce, P. G.; Freunberger, S. A.; Hardwick, L. J.; Tarascon, J.-M. Li-O_2 and Li-S batteries with High Energy Storage. *Nat. Mater.* **2012**, *11*, 19−29.
(6) An, Y.; Fei, H.; Zeng, G.; Xu, X.; Ci, L.; Xi, B.; Xiong, S.; Feng, J.; Qian, Y. Vacuum Distillation Derived 3D Porous Current Collector for Stable Lithium-Metal Batteries. *Nano Energy* **2018**, *47*, 503−511.
(7) An, Y.; Zhang, Z.; Fei, H.; Xu, X.; Xiong, S.; Feng, J.; Ci, L. Lithium Metal Protection Enabled by in-situ Olefin Polymerization for High-Performance Secondary Lithium Sulfur Batteries. *J. Power Sources* **2017**, *363*, 193−198.
(8) Shi, Z. T.; Kang, W.; Xu, J.; Sun, L. L.; Wu, C.; Wang, L.; Yu, Y. Q.; Yu, D. Y. W.; Zhang, W.; Lee, C. S. In situ Carbon-doped $Mo(Se_{0.85}S_{0.15})_2$ Hierarchical Nanotubes as Stable Anodes for High-performance Sodium-ion Batteries. *Small* **2015**, *11*, 5667−5674.
(9) Jiang, Y.; Wei, M.; Feng, J.; Ma, Y.; Xiong, S. Enhancing the Cycling Stability of Na-ion Batteries by Bonding SnS_2 Ultrafine Nanocrystals on Amino-functionalized Graphene Hybrid Nanosheets. *Energy Environ. Sci.* **2016**, *9*, 1430−1438.

DOI: 10.1021/acssuschemeng.8b05904
ACS Sustainable Chem. Eng. 2019, 7, 5921−5930

(10) Kang, H.; Liu, Y.; Cao, K.; Zhao, Y.; Jiao, L.; Wang, Y.; Yuan, H. Update on Anode Materials for Na-ion Batteries. *J. Mater. Chem. A* **2015**, *3*, 17899−17913.
(11) Niu, F.; Yang, J.; Wang, N.; Zhang, D.; Fan, W.; Yang, J.; Qian, Y. $MoSe_2$ Covered N, P doped Carbon Nanosheets as a Long life and High rate Anode Material for Sodium ion Batteries. *Adv. Funct. Mater.* **2017**, *27*, 1700522.
(12) Kang, W.; Wang, Y.; Xu, J. Recent Progress in Layered Metal Dichalcogenide Nanostructures as Electrodes for High-performance Sodium-ion Batteries. *J. Mater. Chem. A* **2017**, *5*, 7667−7690.
(13) Zhao, W.; Guo, C.; Li, C. M. Lychee-like FeS_2@$FeSe_2$ Core−shell Microspheres Anode in Sodium Ion Batteries for Large Capacity and Ultralong Cycle Life. *J. Mater. Chem. A* **2017**, *5*, 19195−19202.
(14) Ong, S. P.; Chevrier, V. L.; Hautier, G.; Jain, A.; Moore, C.; Kim, S.; Ma, X.; Ceder, G. Voltage, Stability and Diffusion Barrier Differences Between Sodium-ion and Lithium-ion Intercalation Materials. *Energy Environ. Sci.* **2011**, *4*, 3680−3688.
(15) You, Y.; Wu, X. L.; Yin, Y. X.; Guo, Y. G. High-quality Prussian Blue Crystals as Superior Cathode Materials for Room-temperature Sodium-ion Batteries. *Energy Environ. Sci.* **2014**, *7*, 1643−1647.
(16) Wang, W.; Shi, L.; Lan, D.; Li, Q. Improving Cycle Stability of SnS Anode for Sodium-ion Batteries by Limiting Sn Agglomeration. *J. Power Sources* **2018**, *377*, 1−6.
(17) Geng, H.; Yang, J.; Dai, Z.; Zhang, Y.; Zheng, Y.; Yu, H.; Wang, H.; Luo, Z.; Guo, Y.; Zhang, Y.; Fan, H.; Wu, X.; Zheng, J.; Yang, Y.; Yan, Q.; Gu, H. Co_9S_8/MoS_2 Yolk−shell Spheres for Advanced Li/Na Storage. *Small* **2017**, *13*, 1603490.
(18) Lu, Z.; Wang, N.; Zhang, Y.; Xue, P.; Guo, M.; Tang, B.; Bai, Z.; Dou, S. Pyrite FeS_2@C Nanorods as Smart Cathode for Sodium Ion Battery with Ultra-Long Life Span and Notable Rate Performance from Tunable Pseudocapacitance. *Electrochim. Acta* **2018**, *260*, 755−761.
(19) Hameed, A. S.; Reddy, M. V.; Chen, J. L. T.; Chowdari, B. V. R.; Vittal, J. J. RGO/Stibnite Nanocomposite as a Dual Anode for Lithium and Sodium Ion Batteries. *ACS Sustainable Chem. Eng.* **2016**, *4*, 2479−2486.
(20) Teng, Y.; Zhao, H.; Zhang, Z.; Zhao, L.; Zhang, Y.; Li, Z.; Xia, Q.; Du, Z.; Swierczek, K. MoS_2 Nanosheets Vertically Grown on Reduced Graphene Oxide via Oxygen Bonds with Carbon Coating as Ultrafast Sodium Ion Batteries Anodes. *Carbon* **2017**, *119*, 91−100.
(21) Xu, Q. T.; Li, J. C.; Xue, H. G.; Guo, S. P. Binary Iron Sulfides as Anode Materials for Rechargeable Batteries: Crystal Structures, Syntheses, and Electrochemical Performance. *J. Power Sources* **2018**, *379*, 41−52.
(22) Wei, X.; Li, W.; Shi, J.; Gu, L.; Yu, Y. FeS@C on Carbon Cloth as Flexible Electrode for both Lithium and Sodium Storage. *ACS Appl. Mater. Interfaces* **2015**, *7*, 27804−27809.
(23) Lee, S. Y.; Kang, Y. C. Sodium Ion Storage Properties of FeS−Reduced Graphene Oxide Composite Powder with a Crumpled Structure. *Chem. - Eur. J.* **2016**, *22*, 2769−2774.
(24) Shao-Horn, Y.; Osmialowski, S.; Horn, Q. C. Nano-FeS_2 for Commercial Li-FeS_2 Primary Batteries. *J. Electrochem. Soc.* **2002**, *149*, A1499−A1502.
(25) Henriksen, G. L.; Vissers, D. R.; Chilenskas, A. A. Safety Characteristics of Lithium Alloy/Metal Sulfide Batteries. *J. Power Sources* **1995**, *54*, 134−137.
(26) Li, L.; Peng, S.; Bucher, N.; Chen, H. Y.; Shen, N.; Nagasubramanian, A.; Eldho, E.; Hartung, S.; Ramakrishna, S.; Srinivasan, M. Large-scale Synthesis of Highly Uniform Fe_{1-x} S Nanostructures as a High-rate Anode for Sodium Ion Batteries. *Nano Energy* **2017**, *37*, 81−89.
(27) Xiao, Y.; Hwang, J. Y.; Belharouak, I.; Sun, Y. K. Na Storage Capability Investigation of a Carbon Nanotube-encapsulated Fe_{1-x} S Composite. *ACS Energy Lett.* **2017**, *2*, 364−372.
(28) Pan, Q.; Zheng, F.; Ou, X.; Yang, C.; Xiong, X.; Tang, Z.; Zhao, L.; Liu, M. MoS_2 Decorated Fe_3O_4/Fe_{1-x} S@C Nanosheets as High-performance Anode Materials for Lithium Ion and Sodium Ion Batteries. *ACS Sustainable Chem. Eng.* **2017**, *5*, 4739−4745.
(29) Jin, P.; Zhang, X.; Wang, J. Mesoporous γ-MnS Nanospheres as Anode Materials for Li-ion Batteries. *Mater. Lett.* **2017**, *188*, 13−16.
(30) Zhang, L.; Zhou, L.; Wu, H. B.; Xu, R.; Lou, X. W. Unusual Formation of Single-Crystal Manganese Sulfide Microboxes Co-mediated by the Cubic Crystal Structure and Shape. *Angew. Chem.* **2012**, *124*, 7379−7382.
(31) Gao, S.; Chen, G.; Dall'Agnese, Y.; Wei, Y.; Gao, Z.; Gao, Y. Flexible MnS−Carbon Fiber Hybrids for Lithium-ion and Sodium-ion Energy Storage. *Chem. - Eur. J.* **2018**, *24*, 13535−13539.
(32) Gao, X.; Zhang, X.; Jiang, J.; Chen, J. Rod-like Carbon-coated MnS Derived from Metal-Organic Frame Works as High-performance Anode Material for Sodium-ion Batteries. *Mater. Lett.* **2018**, *228*, 42−45.
(33) Xu, X.; Ji, S.; Gu, M.; Liu, J. In Situ Synthesis of MnS Hollow Microspheres on Reduced Graphene Oxide Sheets as High-capacity and Long-life Anodes for Li-and Na-ion Batteries. *ACS Appl. Mater. Interfaces* **2015**, *7*, 20957−20964.
(34) Wang, Y.; Kang, W.; Cao, D.; Zhang, M.; Kang, Z.; Xiao, Z.; Wang, R.; Sun, D. A Yolk−shelled Co_9S_8/MoS_2−CN Nanocomposite Derived from a Metal−Organic Framework as a High Performance Anode for Sodium-ion Batteries. *J. Mater. Chem. A* **2018**, *6*, 4776−4782.
(35) Tan, Y.; Liang, M.; Lou, P.; Cui, Z.; Guo, X.; Sun, W.; Yu, X. In Situ Fabrication of CoS and NiS Nanomaterials Anchored on Reduced Graphene Oxide for Reversible Lithium Storage. *ACS Appl. Mater. Interfaces* **2016**, *8*, 14488−14493.
(36) Zhao, L.; Yu, X.; Yu, J.; Zhou, Y.; Ehrlich, S. N.; Hu, Y. S.; Su, D.; Li, H.; Yang, X. Q.; Chen, L. Remarkably Improved Electrode Performance of Bulk MnS by Forming a Solid Solution with FeS − Understanding the Li Storage Mechanism. *Adv. Funct. Mater.* **2014**, *24*, 5557−5566.
(37) Zhu, L.; Chang, Z.; Wang, Y.; Chen, B.; Zhu, Y.; Tang, W.; Wu, Y. Core−shell MnO_2@Fe_2O_3 Nanospindles as a Positive Electrode for Aqueous Supercapacitors. *J. Mater. Chem. A* **2015**, *3*, 22066−22072.
(38) Butler, E. A.; Peters, D. G.; Swift, E. H. Hydrolysis Reactions of Thioacetamide in Aqueous Solutions. *Anal. Chem.* **1958**, *30*, 1379−1383.
(39) Chandra Sekhar, S.; Nagaraju, G.; Yu, J. S. Ant Cave Structured $MnCO_3$/Mn_3O_4 Microcubes by Biopolymer-Assisted Facile Synthesis for High-Performance Pseudocapacitors. *Appl. Surf. Sci.* **2018**, *435*, 398−405.
(40) El Mendili, Y.; Abdelouas, A.; Bardeau, J. F. Insight into the Mechanism of Carbon Steel Corrosion Under Aerobic and Anaerobic Conditions. *Phys. Chem. Chem. Phys.* **2013**, *15*, 9197−9204.
(41) Veerasubramani, G. K.; Subramanian, Y.; Park, M. S.; Nagaraju, G.; Senthilkumar, B.; Lee, Y.-S.; Kim, D.-W. Enhanced Storage Ability by Using a Porous Pyrrhotite@N-doped Carbon Yolk-Shell as an Advanced Anode Material for Sodium-Ion Batteries. *J. Mater. Chem. A* **2018**, *6*, 20056−20068.
(42) Goede, O.; Heimbrodt, W. Optical Properties of (Zn, Mn) and (Cd, Mn) Chalcogenide Mixed Crystals and Super Lattices. *Phys. Status Solidi B* **1988**, *146*, 11−62.
(43) Chou, H.; Fan, H. Y. Light Scattering by Magnons in CoO, MnO and α-MnS. *Phys. Rev. B* **1976**, *13*, 3924−3938.
(44) Anastassiadou, A.; Liarokapis, E.; Anastassakis, E. A Raman Study of Zn_{1-x} Mn_x S Mixed Crystals. *Solid State Commun.* **1989**, *69*, 137−142.
(45) Wang, C.; Lan, M.; Zhang, Y.; Bian, H.; Yuen, M. F.; Ostrikov, K.; Jiang, J.; Zhang, W.; Li, Y. Y.; Lu, J. Fe_{1-x} S/C Nanocomposites from Sugarcane Waste-derived Microporous Carbon for High-performance Lithium Ion Batteries. *Green Chem.* **2016**, *18*, 3029−3039.
(46) Cao, X.; Li, H.; He, J.; Kang, L.; Jiang, R.; Shi, F.; Xu, H.; Lei, Z.; Liu, Z. H. Preparation and Formation Process of a-MnS@MoS_2 Microcubes with Hierarchical Core/shell Structure. *J. Colloid Interface Sci.* **2017**, *507*, 18−26.
(47) Lu, J.; Qi, P.; Peng, Y.; Meng, Z.; Yang, Z.; Yu, W.; Qian, Y. Metastable MnS Crystallites through Solvothermal Synthesis. *Chem. Mater.* **2001**, *13*, 2169−2172.
(48) Wang, Y. X.; Yang, J.; Chou, S. L.; Liu, H. K.; Zhang, W. X.; Zhao, D.; Dou, S. X. Uniform Yolk-shell Iron Sulfide−Carbon Nanospheres for Superior Sodium−Iron Sulfide Batteries. *Nat. Commun.* **2015**, *6*, 8689.

DOI: 10.1021/acssuschemeng.8b05904
ACS Sustainable Chem. Eng. 2019, 7, 5921−5930

(49) Li, Q.; Wei, Q.; Zuo, W.; Huang, L.; Luo, W.; An, Q.; Pelenovich, V. O.; Mai, L.; Zhang, Q. Greigite $Fe_3 S_4$ as a New Anode Material for High-performance Sodium-ion Batteries. *Chem. Sci.* **2017**, *8*, 160−164.
(50) Subramanian, Y.; Park, M. S.; Veerasubramani, G. K.; Lee, Y.-S.; Kim, D.-W. Synthesis and Electrochemical Performance of Carbon-coated $Fe_2 GeO_4$ as an Anode Material for Sodium-Ion Batteries. *Mater. Chem. Phys.* **2019**, *224*, 129−136.
(51) Brezesinski, T.; Wang, J.; Polleux, J.; Dunn, B.; Tolbert, S. H. Templated Nanocrystal-based Porous TiO_2 Films for Next-generation Electrochemical Capacitors. *J. Am. Chem. Soc.* **2009**, *131*, 1802−1809.
(52) Qian, J.; Wu, X.; Cao, Y. L.; Ai, X.; Yang, H. High Capacity, Rate Capability of Amorphous Phosphorus for Sodium Ion Batteries. *Angew. Chem., Int. Ed.* **2013**, *52*, 4633−4636.
(53) Brezesinski, T.; Wang, J.; Tolbert, S. H.; Dunn, B. Ordered Mesoporous α-MoO_3 with Iso-oriented Nanocrystalline Walls for Thin-film Pseudocapacitors. *Nat. Mater.* **2010**, *9*, 146−151.
(54) Kim, W.-S.; Hwa, Y.; Kim, H.-C.; Choi, J.-H.; Sohn, H.-J.; Hong, S.-H. SnO_2@$Co_3 O_4$ Hollow Nano-spheres for a Li-Ion Battery Anode with Extraordinary Performance. *Nano Res.* **2014**, *7* (8), 1128−1136.
(55) Wang, X.; Li, X.; Li, Q.; Li, H.; Xu, J.; Wang, H.; Zhao, G.; Lu, L.; Lin, X.; Li, H.; Li, S. Improved Electrochemical Performance Based on Nanostructured SnS_2@CoS_2-rGO Composite Anode for Sodium-Ion Batteries. *Nano-Micro Lett.* **2018**, *10* (1−12), 46.

DOI: 10.1021/acssuschemeng.8b05904
ACS Sustainable Chem. Eng. 2019, 7, 5921−5930